Industrial Chemistry
& Materials

ROYAL SOCIETY
OF CHEMISTRY

PAPER

View Article Online
View Journal

Check for updates

Cite this: DOI: 10.1039/d5im00294j

Carboxylated cotton fiber-integrated PPy/PANI composites for high-performance flexible supercapacitor electrodes *via* TEMPO oxidation

Meijuan Cao,[a] Xiaopei Wu,[a] Dongdong Qiu,[a] Shouzheng Jiao, *[a] Jian Sun *[b] and Jie Zong[c]

Improving the interfacial interaction between conductive polymers and fiber substrates is essential for developing high-performance flexible supercapacitor electrodes. Herein, a simple and scalable approach is reported to modify cotton fibers *via* TEMPO-mediated oxidation, introducing carboxyl groups onto the fiber surface to produce carboxylated cotton fibers (C-CF). These functional groups significantly enhance the affinity between the fiber substrate and conducting polymers. Sequential *in situ* polymerization of polyaniline (PANI) and polypyrrole (PPy) on C-CF results in a well-integrated composite structure with improved active material loading and optimized multi-scale pore architecture (mesoporous channels together with a preserved open macroporous fiber network). Compared with unmodified fibers, the PPy/PANI/C-CF electrodes exhibit higher porosity, stronger interfacial bonding, and enhanced electrochemical activity. The symmetric flexible supercapacitor exhibits an areal capacitance of 102 μF cm^{-2} and a mass-specific capacitance of 85 mF g^{-1} at an operating voltage of 1.0 V, with an active material loading of 1.2 mg cm^{-2}. The optimized electrode achieves a specific capacitance of 911 F g^{-1} at a current density of 2 mA cm^{-2} and maintains 79.08% capacitance after 1000 cycles, demonstrating cycling stability. This work highlights the effectiveness of fiber surface functionalization *via* TEMPO oxidation in improving electrode structure and performance, offering a promising strategy for flexible energy storage applications.

Received 16th October 2025,
Accepted 3rd April 2026

DOI: 10.1039/d5im00294j

rsc.li/icm

Keywords: TEMPO oxidation; Carboxylated cotton fibers; Conducting polymers; Flexible electrodes; Supercapacitors.

1 Introduction

Flexible supercapacitors require electrode materials that combine high conductivity, mechanical flexibility, and robust electrochemical stability for emerging wearable electronics.[1–4] Cotton fiber (CF) is commonly used as a flexible substrate due to its excellent mechanical strength and biocompatibility, which is distinct from carbon fibers (CarF) widely reported in the existing supercapacitor literature. Conducting polymer composites like polypyrrole (PPy) and polyaniline (PANI) coated on CF have demonstrated synergistic enhancements in electrical conductivity and specific capacitance.[5–7] However, current PPy/PANI/CF electrodes still face critical challenges, including suboptimal high-rate performance and limited cycling stability.[8] One key issue is that coating CF with PPy/PANI increases the active material loading but significantly decreases the electrode's porosity, hindering electrolyte access.[9,10] Another challenge is the weak interfacial bonding between the polymer and CF substrate, stemming from the scarcity of surface functional groups on pristine CF.[11–13] These issues collectively limit the overall electrochemical performance and durability of flexible supercapacitor electrodes.

Surface chemical modification of the CF substrate is a promising strategy to overcome these limitations.[14–16] Among various approaches, 2,2,6,6-tetramethylpiperidine-1-oxyl (TEMPO)-mediated oxidation has emerged as an effective method for introducing carboxyl functional groups into cellulose-based materials.[17–19] The TEMPO oxidation system can selectively oxidize the C6 primary hydroxyls of cellulose to carboxylate groups (–COOH), yielding carboxylated cotton fibers (C-CF).[20–22] This oxidation significantly increases the density of oxygen-containing functional groups on the fiber surface. The introduced –COOH groups provide stronger

---

[a] *Beijing Engineering Research Center of Printed Electronics, School of Printing and Packaging Engineering, Beijing Institute of Graphic Communication, Beijing 102600, P. R. China. E-mail: sz.jiao@outlook.com*

[b] *Key Laboratory of Molecular Medicine and Biotherapy in the Ministry of Industry and Information Technology, School of Life Science, Beijing Institute of Technology, Beijing 100081, China. E-mail: jiansun@bit.edu.cn*

[c] *Department of Chemical Engineering, Engineering and Technology Institute Groningen, University of Groningen, Nijenborgh 4, 9747 AG, Groningen, The Netherlands*

interaction sites (*e.g.*, hydrogen bonding or electrostatic attraction) for the conducting polymers, thereby enhancing interfacial adhesion in the composite.[23,24] In addition, the presence of carboxyl groups improves the wettability and dispersion of the active material on the fibers and can even influence interfiber interactions to maintain a more open porous network.[25,26] Such enhancements in interface bonding and pore structure are expected to translate into superior electrochemical performance for the composite electrodes.

Recent studies report that electro-polymerized polypyrrole electrodes exhibit a specific capacitance of 545 F g^{-1}, while nanofibrous polyaniline electrodes achieve 234 F g^{-1} with 90% capacitance retention after 900 cycles. Polyurethane/MXene electrodes show moderate stability (80.2% retention after 5000 cycles) but a relatively low specific capacitance of 123.2 F g^{-1}. Although polyaniline/graphite paper-based electrodes reach a high capacitance of 1503.7 F g^{-1}, their rigid substrate limits wearable applicability. In stark contrast, our PPy/PANI/C-CF electrode delivers a remarkable specific capacitance of 911 F g^{-1} at a current density of 2 mA cm^{-2}. This value not only surpasses most pure polymer-based fiber electrodes but also maintains a balanced electrochemical performance profile suitable for flexible energy storage systems.

In this work, we capitalize on the advantages of TEMPO oxidation to develop a high-performance flexible electrode. Cotton fibers are first oxidatively modified to introduce abundant –COOH groups, producing C-CF, and then a PPy/PANI coating is deposited onto the C-CF *via in situ* chemical oxidative polymerization. The primary innovation of this work is the resolution of the critical trade-off between active material loading and electrode porosity, a longstanding limitation in previous TEMPO-oxidized cellulose and PANI/PPy fiber electrode research. Unlike conventional single-polymer coatings, the dual PPy/PANI heterostructure on the carboxylated C-CF substrate forms a robust interface *via* covalent and non-covalent interactions, which effectively prevents polymer delamination while preserving the interconnected porous network for rapid ion transport. This design allows a higher loading of active PPy/PANI while preserving the porous structure of the electrode and ensuring strong bonding between the polymer and fiber substrate. As a result, the PPy/PANI/C-CF electrode delivers a high specific capacitance of 911 F g^{-1} at a current density of 2 mA cm^{-2}, along with cycling stability (∼79% capacitance retention after 1000 cycles). These improvements highlight the effectiveness of TEMPO-induced fiber carboxylation in addressing key limitations of flexible supercapacitor electrodes, offering a promising route toward next-generation high-performance energy storage devices.

2 Results and discussion

2.1 Tuning surface chemistry and electrochemical performance of C-CF *via* controlled TEMPO oxidation

To engineer the fiber–polymer interface and promote efficient polymer integration, cotton fibers (CF) were chemically modified using a TEMPO-mediated oxidation system in which sodium hypochlorite (NaClO) served as the primary oxidant (see Fig. 1). This system selectively oxidized the C6 primary hydroxyl groups on cellulose chains into carboxyl groups (–COOH), yielding carboxylated cotton fibers (C-CF) with tunable surface functionality. FTIR spectra (Fig. S1) showed the gradual emergence of a characteristic absorption band at 1605 cm^{-1}, attributed to asymmetric $-COO^-$ stretching, whose intensity increased with NaClO concentration. This indicated a dose-dependent introduction of carboxyl groups. Notably, the presence of COO^- signals—rather than neutral COOH—even after rinsing suggests partial deprotonation or persistent ionic environments on the fiber surface.[27] Meanwhile, XRD analysis (Fig. S2) confirmed that the oxidation did not alter the native crystalline structure of cellulose, as all major peaks corresponding to cellulose I (2θ = 14.7°, 16.5°, 22.6°, and 34.2°) remained unchanged.[28] The presence of carboxyl groups was found to substantially improve the deposition and adhesion of polyaniline (PANI) *via in situ* oxidative polymerization. SEM images (Fig. S3a–f) revealed increasingly uniform and dense polymer coverage with rising oxidant concentration, and the gravimetric weight gain (Fig. S3g) confirmed enhanced PANI loading with more extensive carboxylation. This is attributed to strong hydrogen bonding between the $-NH_2$ groups of aniline and the –COOH moieties introduced on C-CF. However, an increase in oxidant dosage also led to higher sheet resistance (Fig. S3h), suggesting a trade-off between chemical reactivity and electrical continuity. Excessive carboxylation appeared to weaken interfiber cohesion and disrupt conductive pathways, resulting in a more porous and disordered fiber network.

Electrochemical performance evaluation *via* CV, EIS, and GCD measurements (Fig. S4) showed a clear dependence on the oxidation level. The CV curves of PANI/C-CF exhibited enlarged enclosed areas and improved symmetry relative to PANI/CF, with the peak area reaching a maximum at 2 M NaClO (Fig. S4a). EIS analysis revealed that the 2 M sample had the smallest semicircle diameter in the high-frequency region (lowest charge transfer resistance) and the steepest Warburg slope (best ion diffusion; Fig. S4b). The GCD results were consistent with these observations (Fig. S4c and d), with the highest specific capacitance also achieved at the 2 M oxidation level.

From an industrial chemistry perspective, the TEMPO/NaClO-mediated oxidation employed in this work is advantageous in that it is conducted in an aqueous medium under mild conditions and offers selective oxidation of cellulose primary hydroxyl groups. Nevertheless, several practical aspects are relevant for translation and scale-up. First, oxidant consumption and cost are directly tied to the targeted oxidation degree; therefore, operating at an optimized (rather than excessive) NaClO dosage is important to minimize chemical demand while achieving the desired interfacial functionality. Second, environmental and safety considerations primarily relate to hypochlorite handling and

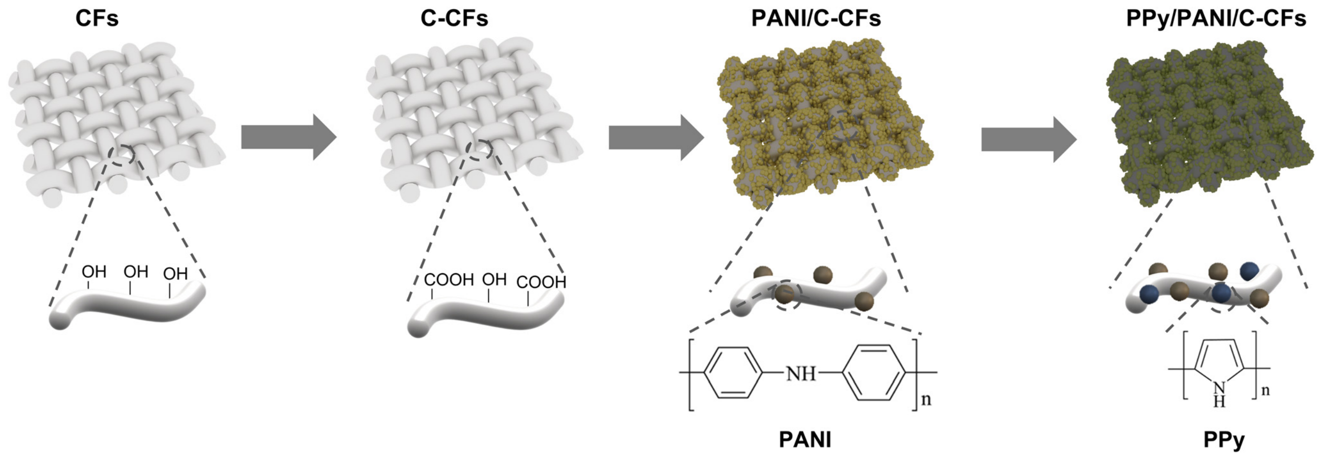

Fig. 1 Schematic illustration of the fabrication process for PPy/PANI/C-CF electrode materials. The procedure includes TEMPO-mediated oxidation of cotton fibers to introduce –COOH groups (C-CF), followed by sequential *in situ* polymerization of aniline (PANI layer) and pyrrole (PPy layer), resulting in a composite electrode with enhanced interfacial interaction, loading capacity, and electrochemical performance.

chloride-containing effluents; in practice, controlled dosing in closed or well-ventilated systems, followed by appropriate quenching/neutralization of residual oxidant and wastewater treatment, would be required. Third, because TEMPO functions catalytically, reuse of the oxidation liquor is conceptually feasible by retaining/recovering the catalyst in the aqueous phase and replenishing only the consumed oxidant/base; however, liquor recycling would require monitoring of residual oxidant, ionic strength (salt accumulation), and byproducts to ensure consistent oxidation

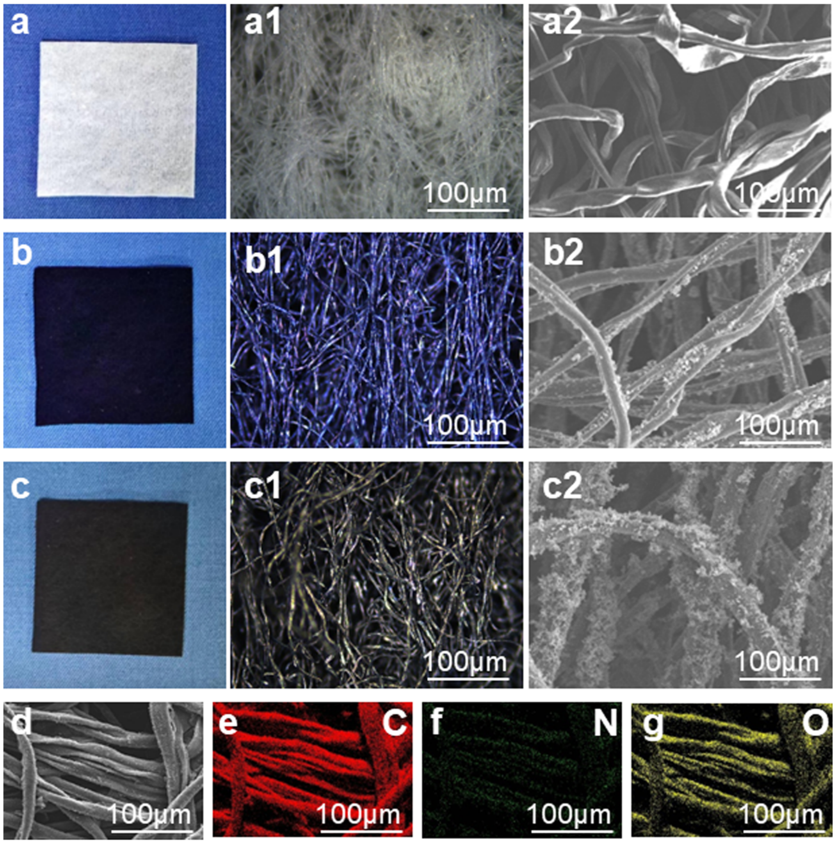

Fig. 2 (a–a2, b–b2, and c–c2) Optical photographs and corresponding SEM images of C-CF, PANI/C-CF, and PPy/PANI/C-CF electrodes, respectively. The increasing polymer loading on the fiber surface is evident through both macroscopic color change and microscopic surface morphology; (d–g) EDS elemental mapping images of PPy/PANI/C-CF, confirming uniform distribution of key elements and successful deposition of the conductive polymer layers.

kinetics. Finally, at larger scale, mass-transfer and mixing limitations (uniform oxidant delivery within fiber bundles), pH control, and heat management can affect reproducibility; these challenges can be mitigated by improved agitation/dispersion, fed-batch oxidant addition, and inline pH control, together with defining a robust specification window (*e.g.*, an oxidation index) for process control.

2.2 Structural and interfacial characterization of PPy/PANI/C-CF electrodes

The sequential *in situ* polymerization of PANI and PPy on carboxylated cotton fibers (C-CF) yielded hierarchical composite electrodes with tunable surface coverage and interfacial architecture. As shown in Fig. 2a–c, the pristine C-CF maintain a white color, whereas both PANI/C-CF and PPy/PANI/C-CF turn uniformly black following polymer deposition, visually confirming the successful coating of conductive polymers. SEM micrographs reveal progressively enhanced polymer loading and surface encapsulation, particularly for the dual-polymer PPy/PANI/C-CF system, which exhibits a dense and continuous conductive layer compared to C-CF alone. To further probe the spatial distribution of polymeric species, elemental mapping *via* energy-dispersive X-ray spectroscopy (EDS) was conducted (Fig. 2d–g). The mapping images of PPy/PANI/C-CF demonstrate uniform distributions of key elements (C, N, O, S), confirming effective and homogeneous deposition of PANI and PPy layers. Compared to PPy/PANI deposited on unmodified CF, the carboxylated substrates provide superior polymer coverage and compositional uniformity, attributed to the enhanced surface polarity and hydrogen-bonding interactions introduced *via* TEMPO oxidation.[29,30]

The interfacial chemical environment was investigated using X-ray photoelectron spectroscopy (XPS), as shown in Fig. 3. The full survey spectra and high-resolution N 1s data (Fig. 3a) reveal a distinct nitrogen signal in polymer-coated samples, while the O 1s peak intensity diminishes, indicating surface masking by nitrogen-rich polymers and partial consumption of oxygen functionalities. High-resolution C 1s spectra (Fig. 3b) exhibit characteristic peaks at 286.7 eV and 288.5 eV in C-CF, corresponding to C═O and O–C═O groups, respectively—confirming the successful introduction of carboxyl groups. After PANI and PPy polymerization, the

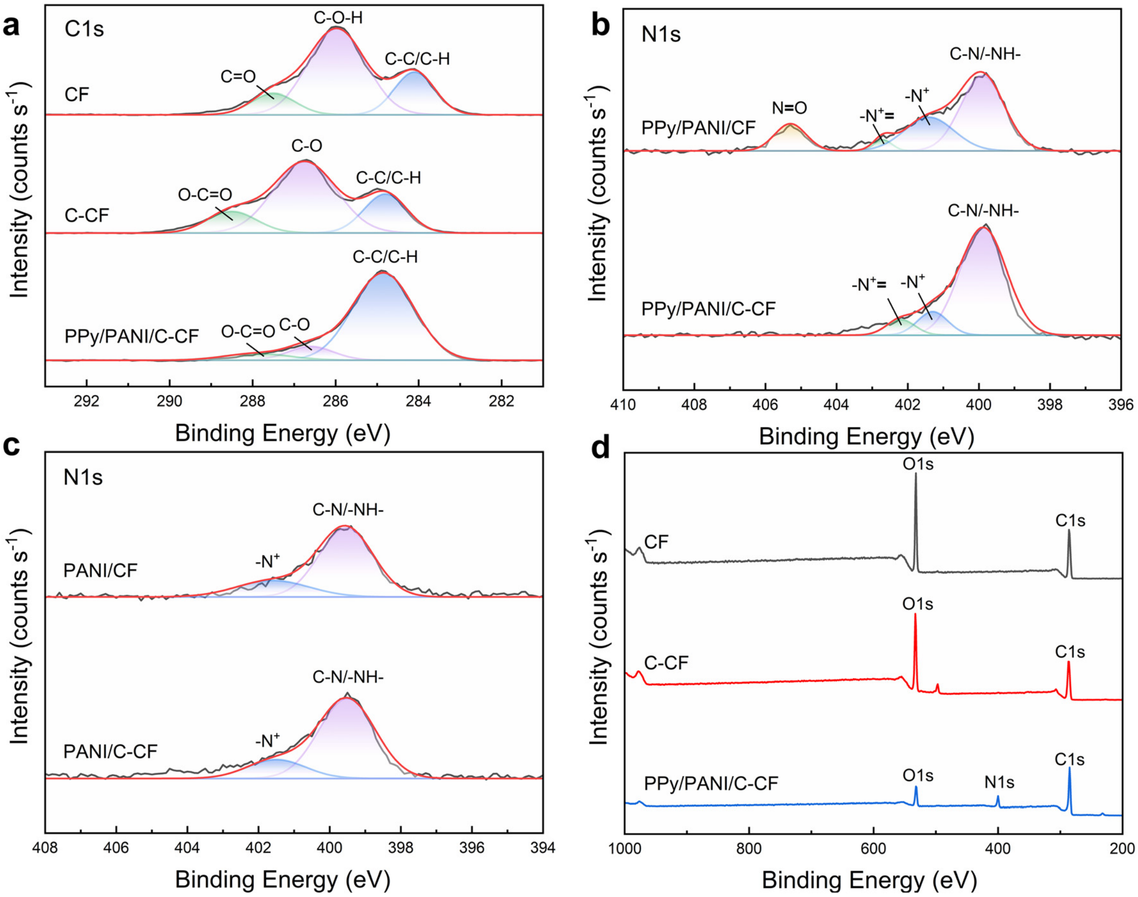

Fig. 3 X-ray photoelectron spectroscopy (XPS) analysis of CF-based electrodes. (a) Full survey spectra and high-resolution N 1s spectra of CF, C-CF, and PPy/PANI/C-CF; (b) high-resolution C 1s spectra comparing CF, C-CF, and PPy/PANI/C-CF, confirming successful carboxylation and polymer interaction; (c) N 1s spectra of PANI/CF and PANI/C-CF, showing enhanced nitrogen signal and protonation after surface modification; (d) N 1s spectra of PPy/PANI/CF and PPy/PANI/C-CF, indicating increased C–N bonding and reduced side reactions with C-CF.

intensities of these peaks are notably reduced, suggesting interfacial reactions between the carboxyl groups and polymer chains. Further evidence of enhanced polymer–substrate interactions is provided by the N 1s spectra. In PANI/C-CF (Fig. 3c), increased signals at 399.5 eV (C–N/–NH–) and 401.5 eV (protonated N^+ species) indicate improved nitrogen bonding and protonation facilitated by surface –COOH groups.[31,32] Similarly, the N 1s spectra of PPy/PANI/C-CF (Fig. 3d) exhibit intensified C–N bonding and an absence of N=O by-products, implying fewer oxidative side reactions and more controlled polymer growth when C-CF are used as substrates.

To provide a quantitative descriptor of the TEMPO-induced surface oxidation, we extracted a semi-quantitative "carboxylation index" from the C 1s peak deconvolution, defined as the fractional area of the O–C=O component, $f_{\mathrm{O-C=O}} = A_{\mathrm{O-C=O}}/\sum A_{\mathrm{C\ 1s}}$. Using this metric, the O–C=O fraction increases from 0.2% for pristine CF to 4.6% for TEMPO-oxidized C-CF, indicating a substantial enrichment of carboxyl-related functionalities on the fiber surface. Notably, the PPy/PANI/C-CF electrode still exhibits an appreciable O–C=O contribution (3.2%), consistent with the retention of carboxyl-related interfacial functionalities after polymer deposition. It should be noted that XPS probes only the near-surface region (a few nanometers); therefore, $f_{\mathrm{O-C=O}}$ is used here as a quantitative descriptor of surface carboxyl enrichment rather than an absolute bulk –COOH content in mmol g^{-1}.

In addition to chemical modifications, the impact of surface carboxylation on the physical microstructure was assessed through porosity measurements (Fig. 4). In addition, N_2 adsorption–desorption measurements (Fig. S7b) show a BET specific surface area of 1.2163 $m^2\ g^{-1}$ and a BJH average pore diameter of 29.9030 nm (desorption branch), indicating mesoporous features that complement the macroporous interfiber voids in the nonwoven network. The PPy/PANI/C-CF electrode displays a porosity of 87.36%, slightly higher than that of its unmodified counterpart (86.40%). This enhancement is attributed to the disruption of interfiber hydrogen bonding during TEMPO oxidation, which loosens the fiber network, facilitating electrolyte infiltration and improving ionic transport—an essential prerequisite for efficient electrochemical performance.[33]

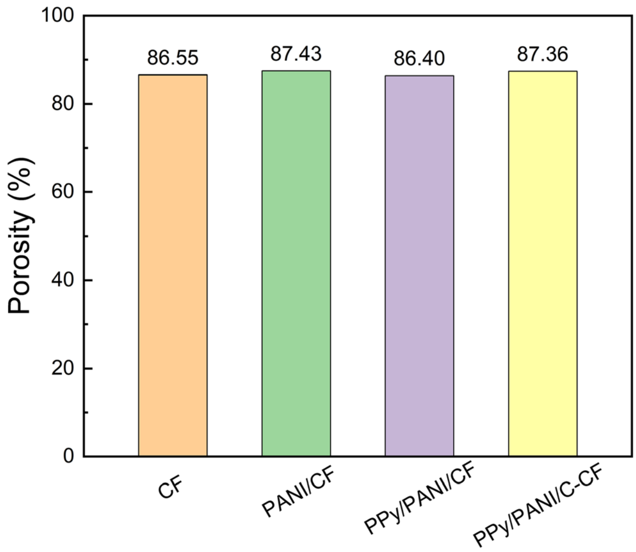

Fig. 4 Comparison of porosity among CF, PANI/CF, PPy/PANI/CF, and PPy/PANI/C-CF. The introduction of carboxyl groups *via* TEMPO oxidation leads to a looser fiber structure, enhancing the porosity of PPy/PANI/C-CF and facilitating improved electrolyte penetration and ion transport.

2.3 Effect of Py : ANI ratio and dopant type on the electrochemical performance of PPy/PANI/CF electrodes

To identify the optimal composition and elucidate the synergistic effect between PPy and PANI, we first investigated PPy/PANI/CF electrodes fabricated with different Py : ANI ratios. Fig. 5a compares the CV curves recorded at 50 mV s^{-1}. The PANI/CF electrode exhibits a relatively wider usable potential window but a less symmetric CV profile, whereas the PPy/CF electrode shows a more symmetric response with a comparatively narrower potential window. Notably, the PPy/PANI hybrid electrodes integrate the advantages of both components, yielding an improved balance between the accessible potential range and the symmetry of the capacitive response, which is desirable for stable electrochemical operation over a wider voltage range. Among the tested compositions, the electrode with Py : ANI = 0.5 : 0.5 delivers the largest enclosed CV area, suggesting the most favorable charge-storage capability.

The EIS results (Fig. 5b) further support this trend. In the high-frequency region, the PANI/CF electrode presents a larger semicircle than the PPy/CF electrode, indicating a higher charge-transfer resistance for PANI/CF. In the low-frequency region, the PPy/CF electrode exhibits a steeper line, implying a lower ion-diffusion impedance than PANI/CF. After combining PPy and PANI, the PPy/PANI/CF electrodes show a reduced semicircle and a steeper low-frequency line compared with PANI/CF, evidencing simultaneously improved interfacial charge transfer and ion transport. Consistently, the Py : ANI = 0.5 : 0.5 electrode shows a comparatively small semicircle and the steepest low-frequency slope, indicating more favorable capacitive kinetics.

Fig. 5c and d display the GCD curves (2 mA cm^{-2}) and the derived specific capacitances, respectively. In agreement with the CV and EIS analyses, the PPy/PANI/CF electrodes benefit from the synergistic interaction between PPy and PANI, and the Py : ANI = 0.5 : 0.5 electrode exhibits the longest discharge time and the highest specific capacitance among the investigated ratios, confirming it as the optimal composition for subsequent studies.

The electrochemical performance of PPy/PANI/CF electrodes can be further regulated by the dopant chemistry. Fig. 6a shows the CV curves of PPy/PANI/CF electrodes prepared using different dopants at 50 mV s^{-1}. The electrode

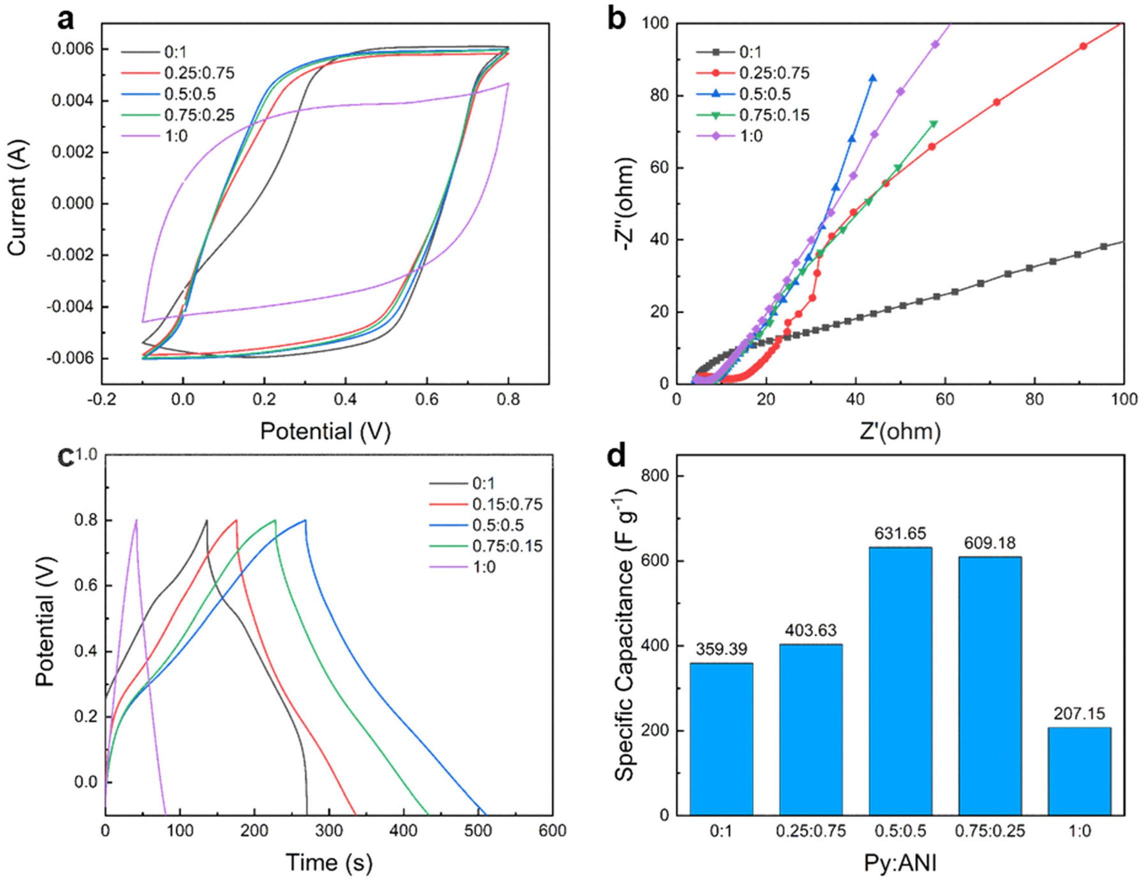

Fig. 5 Electrochemical performance of PPy/PANI/CF electrodes prepared with different Py : ANI ratios. (a) CV curves at 50 mV s^{-1}, (b) EIS Nyquist plots, (c) GCD curves at 2 mA cm^{-2}, and (d) corresponding specific capacitances.

doped with *p*-TSA exhibits the largest CV area and a wide, highly symmetric voltage window, indicating superior capacitive behavior. In comparison, the HCl-doped electrode displays a smaller CV area, while the electrodes doped with SDBS, lignosulfonate, and CTAB show narrower voltage windows and poorer symmetry, suggesting less favorable electrochemical characteristics.

The EIS spectra (Fig. 6b) reveal dopant-dependent charge-transfer and diffusion behaviors. In the high-frequency region, SDBS-, lignosulfonate-, and CTAB-doped electrodes show relatively larger semicircles, whereas the *p*-TSA- and HCl-doped electrodes exhibit smaller semicircles, indicating lower charge-transfer resistance. Among them, the *p*-TSA-doped electrode presents the smallest semicircle. In the low-frequency region, the *p*-TSA-doped electrode shows a markedly steeper line than the others, implying the lowest diffusion impedance and the most efficient ion transport.

The GCD profiles (Fig. 6c) and the corresponding specific capacitances (Fig. 6d) are consistent with the above observations: the *p*-TSA-doped PPy/PANI/CF electrode delivers the longest discharge time and the highest specific capacitance, demonstrating that *p*-TSA is the most effective dopant among those tested for achieving optimal electrochemical performance.

2.4 Effect of oxidant dosage on the morphology and electrochemical performance of PPy/PANI/C-CF electrodes

To further investigate the role of surface functionalization in tuning composite electrode performance, C-CF prepared with different NaClO concentrations were used as substrates for the sequential deposition of PANI and PPy. SEM images (Fig. S5a–f) reveal a marked increase in the deposition of the PPy/PANI composite with increasing levels of carboxylation. Compared to unmodified CF, C-CF enable more uniform and denser polymer coatings, attributed to the enhanced interfacial affinity provided by the –COOH groups. Quantitative weight gain analysis (Fig. S5g) shows a monotonic increase in polymer loading with increasing oxidant concentration, reaching a maximum of 24.24% at 5 M NaClO.

Interestingly, electrical conductivity follows a non-monotonic trend. As shown in Fig. S5h, sheet resistance first decreases and then increases with increasing oxidation level, reaching a minimum of 139.9 Ω sq^{-1} at 2 M NaClO. At low oxidation levels, the limited carboxyl group content reduces polymer adhesion, leading to sparse and discontinuous coatings. At high oxidation levels (≥3 M), excessive polymer accumulation may result in the formation of densely packed, poorly connected polymer domains, which obstruct electron pathways and degrade overall conductivity.

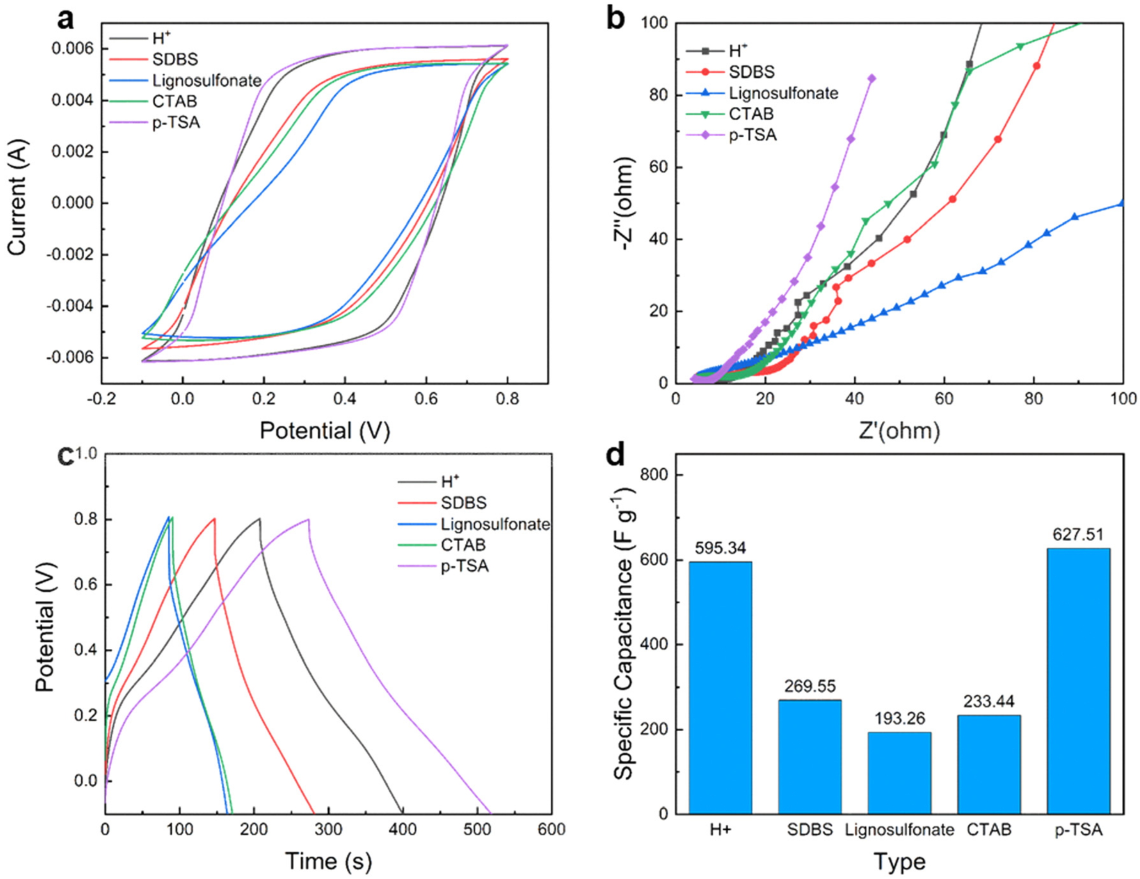

Fig. 6 Electrochemical performance of PPy/PANI/CF electrodes prepared with different dopants (HCl, SDBS, lignosulfonate, CTAB, and *p*-TSA). (a) CV curves at 50 mV s^{-1}, (b) EIS Nyquist plots, (c) GCD curves at 2 mA cm^{-2}, and (d) corresponding specific capacitances.

The electrochemical performance of the resulting PPy/PANI/C-CF electrodes was evaluated using cyclic voltammetry (CV), electrochemical impedance spectroscopy (EIS), and galvanostatic charge–discharge (GCD) measurements. As shown in Fig. S6a, CV profiles exhibit significantly enlarged areas and improved redox symmetry for C-CF-based electrodes relative to PPy/PANI/CF, with the highest current response observed at 1 M NaClO. Beyond this level, the CV area progressively declines, suggesting that mild carboxylation facilitates effective charge storage, while excessive oxidation disrupts the polymer–electrolyte interface or polymer morphology.

EIS results (Fig. S6b) are consistent with these findings. While high-frequency semicircle diameters remain relatively constant across samples, the low-frequency region—indicative of ion diffusion—shows marked variation. The electrode prepared with 1 M NaClO exhibits the steepest Warburg slope and the smallest charge-transfer resistance, indicating the most favorable ion transport and interface kinetics. GCD results (Fig. S6c and d) further confirm this trend, with both discharge time and specific capacitance peaking at the 1 M condition. Under these optimal conditions, the PPy/PANI/C-CF electrode achieves a maximum specific capacitance of 911.0 F g^{-1}, demonstrating superior charge storage capability (other relevant data have been supplemented in Table S2).

To assess rate performance and reversibility, CV and GCD measurements were carried out at various scan rates and current densities (Fig. 7a–d). The CV curves (Fig. 7a) maintain recognizable redox peaks up to 20 mV s^{-1}, beyond which peak distortion becomes evident due to polarization. The GCD profiles (Fig. 7b) remain symmetric across different current densities, indicating good electrochemical reversibility.[34,35] As shown in Fig. 7c and d, the specific capacitance decreases with increasing current density but retains 62.14% of its initial value at 10 mA cm^{-2}, confirming excellent rate capability.

Since NaClO concentration is the key parameter for optimization, we further constructed an explicit structure–property correlation by linking the oxidation degree (quantified by the XPS-derived carboxylation index $f_{\mathrm{O-C=O}}$, summarized in Table S1) with polymer loading, electronic transport, and capacitive performance. As the NaClO dosage increases, $f_{\mathrm{O-C=O}}$, indicating a higher density of carboxyl-related surface functionalities that promotes polymer anchoring and thus increases polymer loading (gravimetric mass gain, Fig. S5g). However, conductivity-related metrics (four-point-probe sheet resistance and/or charge-transfer resistance) exhibit a

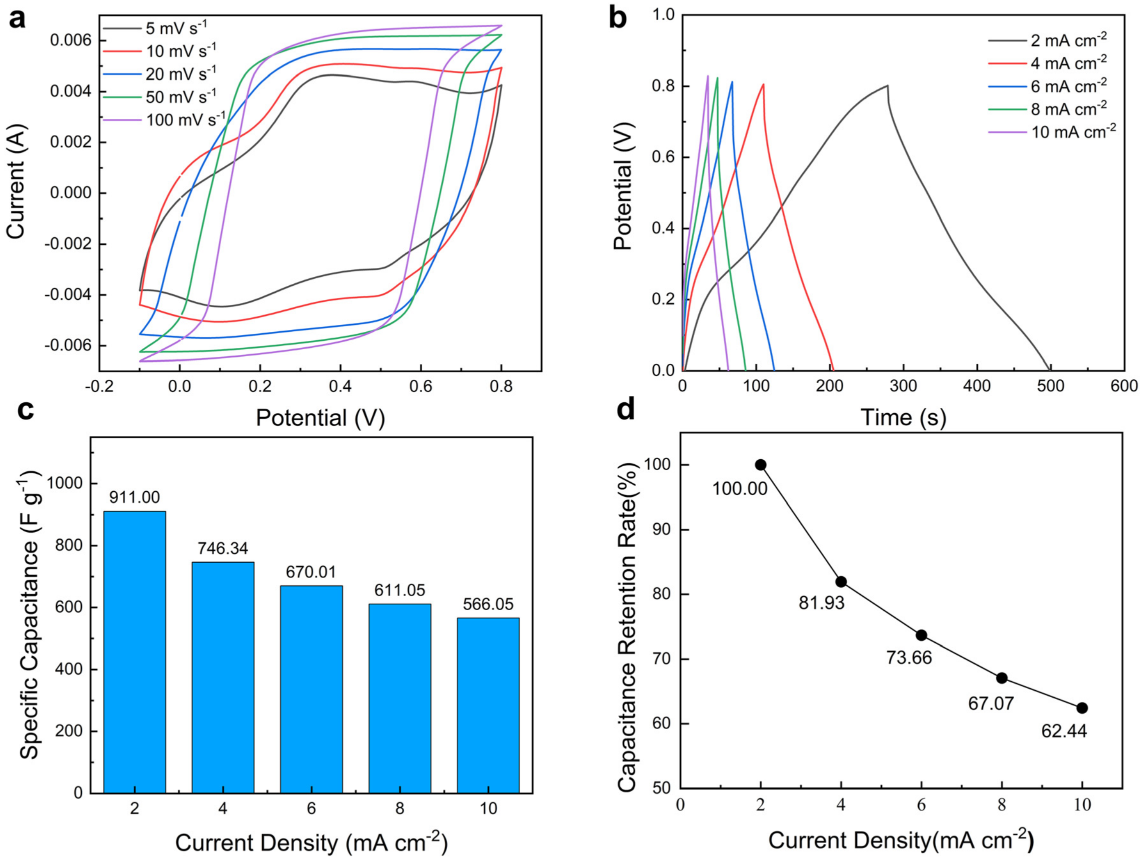

Fig. 7 Electrochemical performance of PPy/PANI/C-CF electrodes. (a) CV curves at different scan rates (5–100 mV s^{-1}), showing current responsiveness and redox behavior; (b) GCD curves at varying current densities, illustrating electrochemical reversibility; (c) specific capacitance values derived from GCD data; (d) rate performance expressed as capacitance retention across current densities. The results confirm the excellent rate capability and stable charge–discharge behavior of the PPy/PANI/C-CF electrode.

non-monotonic dependence on oxidation level, reflecting a trade-off between improved interfacial adhesion/loading and preserved electronic percolation/transport pathways. Consistently, the specific capacitance does not increase monotonically with oxidation degree; instead, the best capacitive performance is achieved at an intermediate oxidation level where polymer loading is sufficiently high while charge/ion transport remains favorable. This quantitative correlation substantiates that NaClO optimization is governed by a balance among surface carboxylation (oxidation degree), polymer loading, conductivity/transport kinetics, and capacitance.

To further elucidate the charge-storage mechanism of the PPy/PANI/C-CF electrode, kinetic analyses were conducted using CV data acquired at scan rates from 5 to 100 mV s^{-1}. The relationship between peak (or representative) current (i) and scan rate (v) was evaluated using the power-law equation $i = av^b$, where $b = 0.5$ and $b = 1$ correspond to diffusion-controlled and surface-controlled processes, respectively. The extracted b values fall between 0.5 and 1, indicating mixed charge-storage kinetics involving both capacitive-controlled and diffusion-influenced pseudocapacitive contributions. This behavior is consistent with the retention of recognizable redox features at relatively low scan rates and the increasing polarization at higher scan rates.

To quantify the relative contributions, Dunn's method was further applied according to $i(V) = k_1v + k_2v^{1/2}$, where k_1v represents the capacitive-controlled current and $k_2v^{1/2}$ corresponds to diffusion-related processes. The capacitive fraction increases with scan rate, indicating that the electrode progressively operates under surface-controlled kinetics at high rates. Moreover, the enhanced porous architecture facilitating electrolyte infiltration and the improved ion-transport/interfacial kinetics evidenced by EIS (steeper Warburg region and reduced charge-transfer resistance under optimized oxidation) together account for the improved rate capability of the PPy/PANI/C-CF electrode.

2.5 Electrochemical stability and long-term cycling performance

To assess the durability of the composite electrodes under prolonged cycling, galvanostatic charge–discharge tests were conducted over 1000 cycles. As shown in Fig. 8a, the PANI/C-CF electrode retains 78.82% of its initial capacitance at a current density of 1 mA cm^{-2}, a notable improvement over its unmodified counterpart (PANI/CF), which exhibits significantly faster degradation. Similarly, the PPy/PANI/C-CF electrode demonstrates superior long-term stability, retaining 79.08% of its initial capacitance after 1000 cycles at 10 mA cm^{-2} (Fig. 8b), outperforming the PPy/PANI/CF control. These results clearly highlight the beneficial role of surface carboxylation in stabilizing the polymer–fiber interface. The presence of –COOH groups enhances interfacial adhesion and suppresses delamination or structural collapse during repeated charge–discharge cycling. Moreover, the more homogeneous polymer distribution and improved porosity provided by the C-CF substrate likely facilitate stress dissipation and ion buffering, further contributing to improved mechanical and electrochemical resilience (Fig. 8).[36]

2.6 Electrochemical performance and interface kinetics of PPy/PANI/C-CF flexible supercapacitors

Systematic electrochemical characterizations including nitrogen adsorption–desorption, electrochemical impedance spectroscopy (EIS), galvanostatic charge–discharge (GCD) and Ragone plot analysis were carried out to elucidate the pore structure characteristics, charge/ion transfer kinetics and energy-power density performance of the devices (Fig. 9a and b). This structure is a synergistic result of the macroporous inter-fiber voids of C-CF nonwoven network, the mesopores formed by PANI/PPy polymer aggregation and the micropores generated during *in situ* polymerization. The hierarchical porous structure not only provides a large specific surface area to expose abundant electroactive sites for pseudocapacitive reaction and electric double layer capacitance formation, but also constructs a continuous and unobstructed transport channel for electrolyte ions, which effectively reduces ion diffusion resistance and lays a structural foundation for the excellent electrochemical performance of the supercapacitor. EIS measurements were performed on the assembled symmetric devices, and the Nyquist impedance plot was fitted with an equivalent circuit model consisting of series resistance (R_s), charge transfer resistance (R_{ct}) and Warburg impedance (W) (Fig. 9c) to quantitatively analyze the interface kinetics and ion transport behavior of the electrode. The experimental Nyquist curve of PPy/PANI/C-CF electrode exhibited a small semicircle in the high-frequency region and a nearly vertical straight line in the low-frequency region, and the fitting curve was highly consistent with the experimental data, verifying the rationality of the equivalent circuit model and the reliability of impedance analysis. The small high-frequency semicircle diameter indicated a low R_{ct} at the electrode–electrolyte interface, which was attributed to the good electrical conductivity of PPy/PANI dual conductive polymer layer and the tight interfacial combination between polymer and C-CF substrate, effectively reducing the contact resistance between components. The nearly vertical low-frequency curve reflected the ideal capacitive behavior of the composite electrode, and the steep Warburg slope indicated fast ion diffusion kinetics in the electrode interior and at the interface, which was consistent with the results of nitrogen adsorption–desorption test that the electrode had a developed hierarchical porous structure. The low R_s and R_{ct} as well as fast ion diffusion characteristics ensure the rapid progress of electrochemical reaction, which is the key to the excellent rate performance and high power density of PPy/PANI/C-CF supercapacitor. Based on the GCD test results at 1–10 mA cm^{-2}, the energy density (E) and power density (P) of the supercapacitor were calculated according to the formulas $E = \left(\frac{1}{2}\right) \times C \times \frac{\Delta V^2}{3.6}$ and $P = (E \times 3600)/\Delta t$ and a Ragone plot was constructed to compare the energy-power density performance with that of recently reported state-of-the-art flexible supercapacitors (Fig. 9d). The PPy/PANI/C-CF supercapacitor prepared in this work exhibited a more balanced and superior energy-power density performance compared with reported flexible supercapacitors such as wrinkled graphene films-SC,

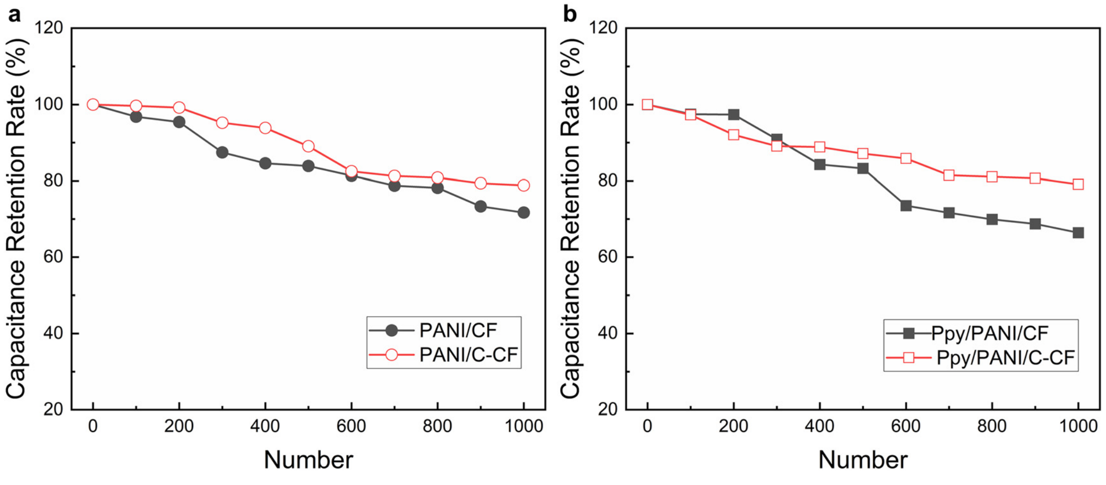

Fig. 8 Cycling stability of electrode materials. (a) Capacitance retention of PANI/CF and PANI/C-CF electrodes at a current density of 1 mA cm^{-2}; (b) capacitance retention of PPy/PANI/CF and PPy/PANI/C-CF electrodes at 10 mA cm^{-2} over 1000 charge–discharge cycles. The C-CF-based electrodes exhibit significantly improved stability, demonstrating the beneficial effect of carboxylation on long-term electrochemical performance.

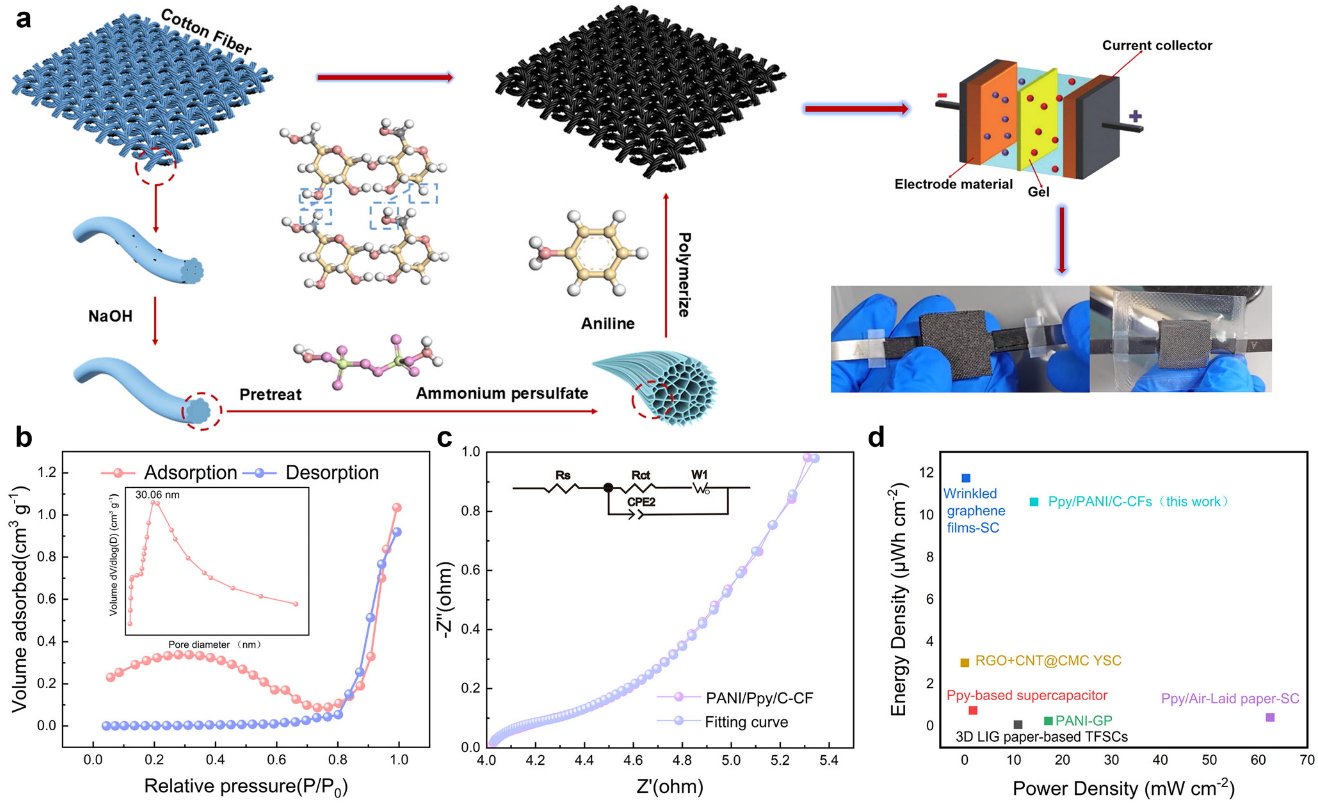

Fig. 9 Preparation, characterization, and electrochemical performance of the electrode material. (a) Schematic illustration of the fabrication process for the PANI/Ppy/C-CFs composite electrode and the assembly of the flexible solid-state supercapacitor; (b) Nitrogen adsorption–desorption isotherms of the flexible PANI/Ppy/C-CFs electrode material (the inset shows the pore size distribution curve); (c) Nyquist impedance plot and the corresponding fitting curve of the PANI/Ppy/C-CFs electrode; (d) Ragone plot comparing the energy density and power density performance of the PANI/Ppy/C-CFs supercapacitor (this work) with those of recently reported electrode materials.

Table 1 Performance comparison of recent flexible supercapacitor electrode materials

Material category	Specific/areal capacitance	Energy density	Power density	Cycling stability
Electropolymerized polypyrrole-based electrode	545 F g^{-1}	—	—	—
Flexible polyaniline–carbon nanofiber supercapacitor electrodes	234 F g^{-1}	32 Wh kg^{-1}	500 W kg^{-1}	90%
Polyurethane/MXene electrodes	123.2 F g^{-1}	4.8 Wh kg^{-1}	630.8 W kg^{-1}	80.2%@5000
Au fabric electrodes	495 mF cm^{-2}	33 μWh cm^{-2}	10 660 μW cm^{-2}	
Polyaniline/graphite paper-based electrodes	1503.7 F g^{-1}	5.7 Wh kg^{-1}	6000 W kg^{-1}	86@15 000
The graphene papers based electrodes	54.5 mF cm^{-2}	10.9 μWh cm^{-2}	—	86.9@15 000
Nanofibrous polypyrrole electrodes	4817.9 mF cm^{-2}	14.6 Wh kg^{-1}	174.6 W kg^{-1}	—
PEDOT/flexible paper based electrodes	639 mF cm^{-2}	—	—	—
Low-oxidized graphene/polyaniline/porous carbon ternary composites	162 mF cm^{-2}	24.9 μWh cm^{-2}	—	90%@thousands of times

RGO + CNT@CMC, PPy-based supercapacitor, PPy/air-laid paper-SC, PAN/Ppy/C-CF, PANI-GP and 3DLIG paper-based TFSCs (Table 1); the PPy/PANI dual polymer layer forms a complementary conductive network, which not only increases the pseudocapacitive contribution of the electrode, but also improves the overall electrical conductivity; the hierarchical porous structure optimizes the ion transport path and shortens the ion diffusion distance. The above advantages make the PPy/PANI/C-CF supercapacitor break through the performance trade-off between energy density and power density of traditional flexible supercapacitors, showing great application potential in wearable electronic devices.

2.7 Mechanical flexibility and electrochemical stability under repeated bending

For flexible supercapacitors applied in wearable and portable electronic devices, excellent mechanical flexibility and electrochemical stability under repeated mechanical deformation are crucial practical performance indicators.

Therefore, we conducted repeated mechanical bending tests on PPy/PANI/C-CF flexible supercapacitors (bending angle of 90°, bending cycle of 1000 times), and performed scanning electron microscopy (SEM), cyclic voltammetry (CV), and constant current charge discharge (GCD) tests at various scanning rates and current densities to systematically compare and analyze the electrochemical performance before and after bending (Fig. 11–13), in order to comprehensively evaluate the mechanical flexibility and structural stability of the composite electrode. After cyclic bending, the electrode morphology transitions from a compact state with agglomerated and coated active material (Fig. 10a) to a fluffy state characterized by fiber bending and entanglement, as well as dispersed and peeled active material (Fig. 10b). Although this structural evolution optimizes the electrolyte permeation channels, the partial detachment of active material and the fracture of the conductive network directly lead to reduced electron transport efficiency and a decrease in effective active sites, ultimately manifesting as a decline in electrochemical performance. This underscores the importance of enhancing the interfacial bonding strength between fibers and active material for the cyclic stability of flexible devices. The CV curves of the supercapacitor at scan rates of 5–100 mV s^{-1} in the initial unbent state (Fig. 11a and 12a) all exhibited a nearly ideal rectangular shape without obvious redox peak distortion, which is the characteristic of the synergistic effect of electric double layer capacitance from C-CF porous structure and pseudocapacitance from PPy/PANI conductive polymers. With the increase of scan rate from 5 mV s^{-1} to 100 mV s^{-1}, the CV curves still maintained a well-defined rectangular shape without obvious polarization, indicating the excellent rate performance of the PPy/PANI/C-CF supercapacitor under static conditions. After 1000 cycles of 90° mechanical bending (Fig. 11b and 12b), the CV curves at the same scan rate range still retained the nearly ideal rectangular shape consistent with the unbent state, without obvious deformation, polarization or reduction of the enclosed area. The comparative CV curves at individual scan rates (5, 10, 20, 50, 100 mV s^{-1}) before and after bending (Fig. 12c–g) showed highly overlapping trends, with no significant difference in current response and curve shape. Even at a high scan rate of 100 mV s^{-1}, the CV curves before and after bending still overlapped closely, indicating that the PPy/PANI/C-CF supercapacitor has outstanding electrochemical stability against repeated mechanical bending. The GCD performance of the supercapacitor before and after repeated bending was further investigated at different current density ranges (Fig. 11c, d and 13). The GCD curves of the unbent supercapacitor at current densities of 2–10 A cm^{-2} (Fig. 11c) and 1–10 A cm^{-2} (Fig. 13a) all presented a nearly symmetrical triangular shape, with no obvious voltage drop (IR drop) at the initial stage of discharge, reflecting the excellent charge–discharge reversibility and low internal resistance of the device, which is consistent with the EIS test results. After 1000 cycles of 90° bending, the GCD curves at the same current density ranges (2–10 A cm^{-2}, Fig. 11d; 1–10 A cm^{-2}, Fig. 13b) still retained the symmetrical triangular profile, and the comparative GCD curves at individual current densities (1, 2, 4, 6, 10 A cm^{-2}) before and after bending (Fig. 13c–g) showed differences in discharge time, voltage drop and curve symmetry. The specific capacitance calculated from GCD curves had no obvious attenuation after repeated bending, which further confirmed the stable charge–discharge behavior of the supercapacitor under mechanical deformation conditions.

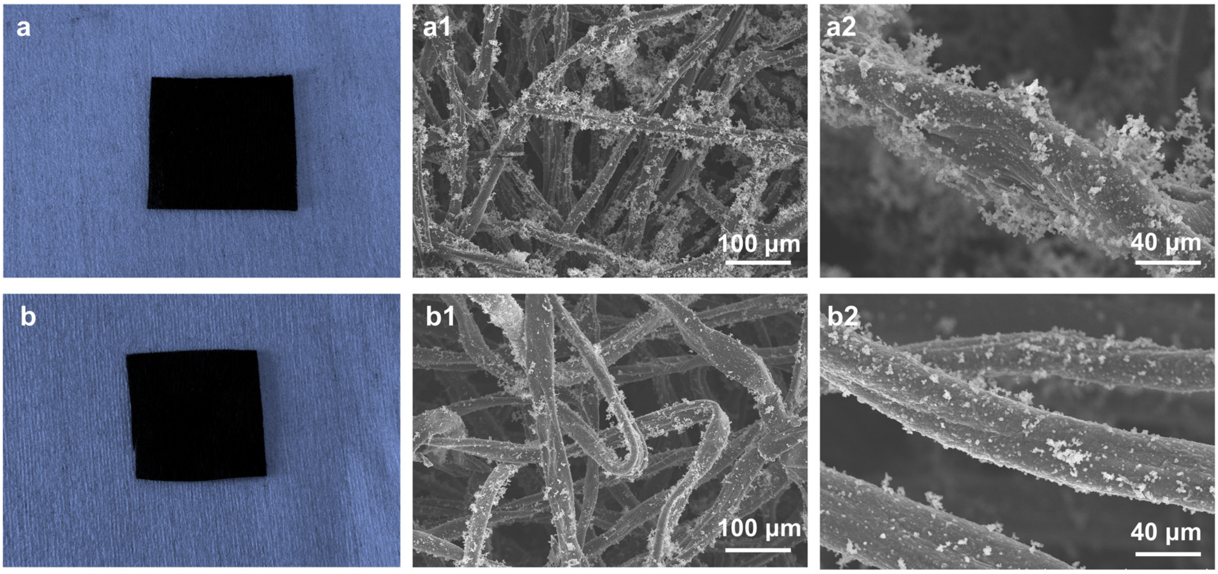

Fig. 10 SEM characterizations of PPy/PANI/C-CF electrodes before (a–a2) and after (b–b2) 1000 bending cycles. (a and b) Optical photographs of the electrodes; (a1 and b1) low-magnification SEM images (scale bar: 100 μm); (a2 and b2) high-magnification SEM images (scale bar: 40 μm).

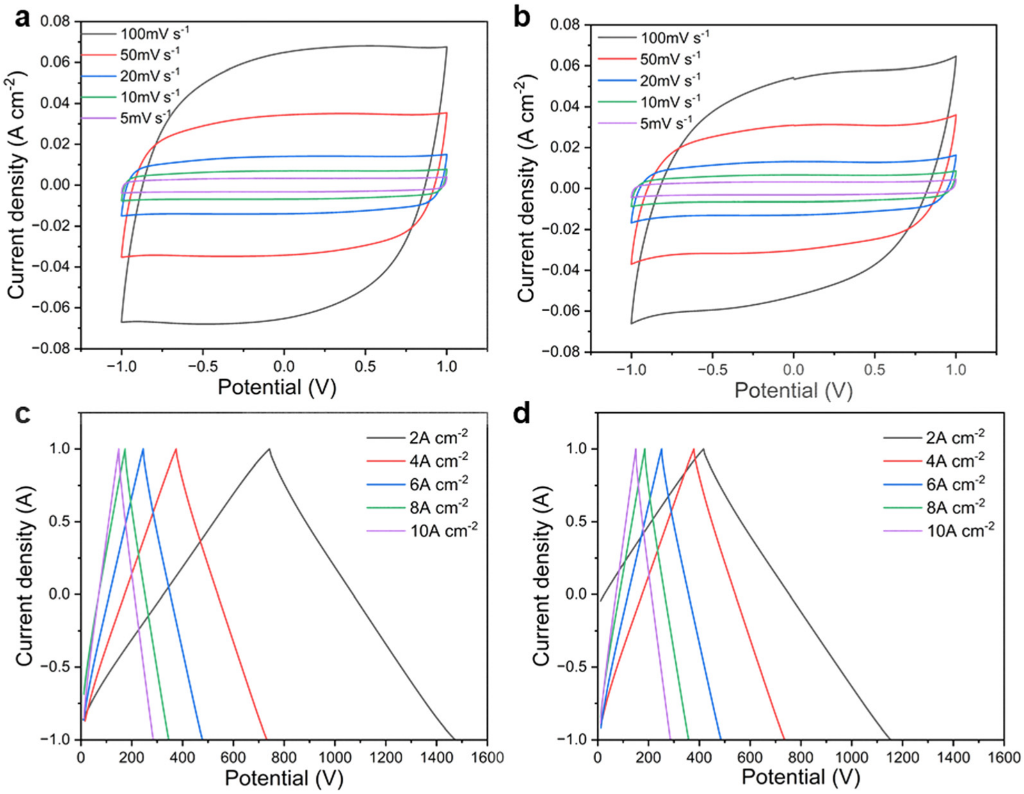

Fig. 11 Electrochemical performance of the flexible supercapacitor before and after repeated mechanical bending. (a) Cyclic voltammetry (CV) curves of the flexible supercapacitor at various scan rates (5–100 mV s^{-1}) in the initial, unbent state; (b) cyclic voltammetry (CV) curves of the flexible supercapacitor at various scan rates (5–100 mV s^{-1}) after repeated mechanical bending (90° bending angle, 1000 bending cycles); (c) galvanostatic charge–discharge (GCD) curves of the flexible supercapacitor at different current densities (2–10 A cm^{-2}) in the initial, unbent state; (d) galvanostatic charge–discharge (GCD) curves of the flexible supercapacitor at different current densities (2–10 A cm^{-2}) after repeated mechanical bending (90° bending angle, 1000 bending cycles).

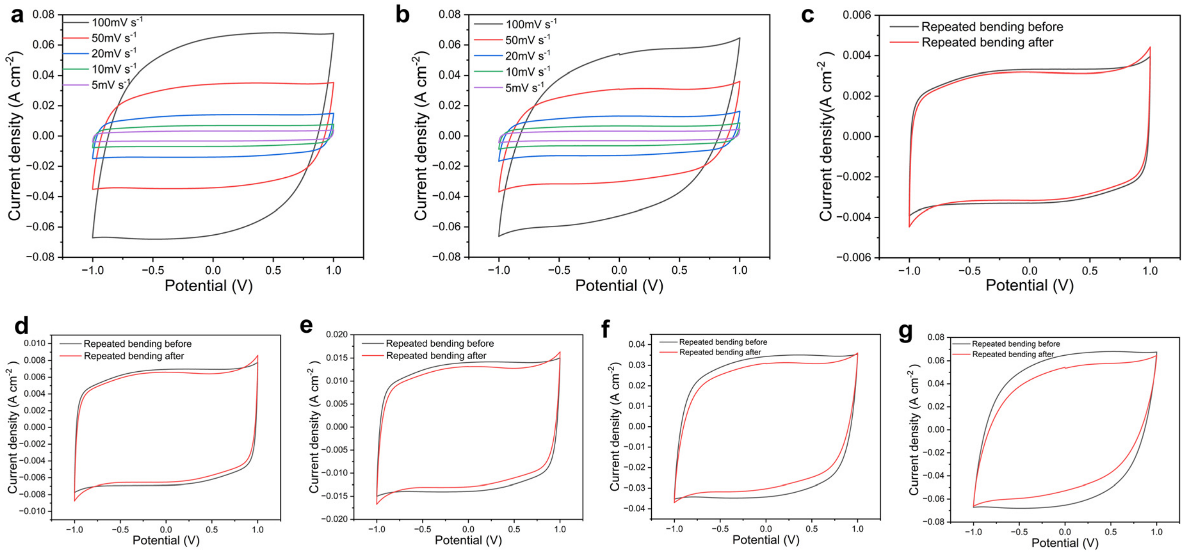

Fig. 12 Electrochemical stability of the flexible supercapacitor under repeated bending conditions. (a) Cyclic voltammetry (CV) curves of the flexible supercapacitor at various scan rates (5–100 mV s^{-1}) in the initial, unbent state; (b) cyclic voltammetry (CV) curves of the flexible supercapacitor at various scan rates (5–100 mV s^{-1}) after repeated mechanical bending (90° bending angle, 1000 bending cycles); (c–g) comparative cyclic voltammetry (CV) curves at scan rates of 5, 10, 20, 50, and 100 mV s^{-1}, respectively, showing the electrochemical performance before (black curves) and after (red curves) repeated mechanical bending (90° bending angle, 1000 bending cycles).

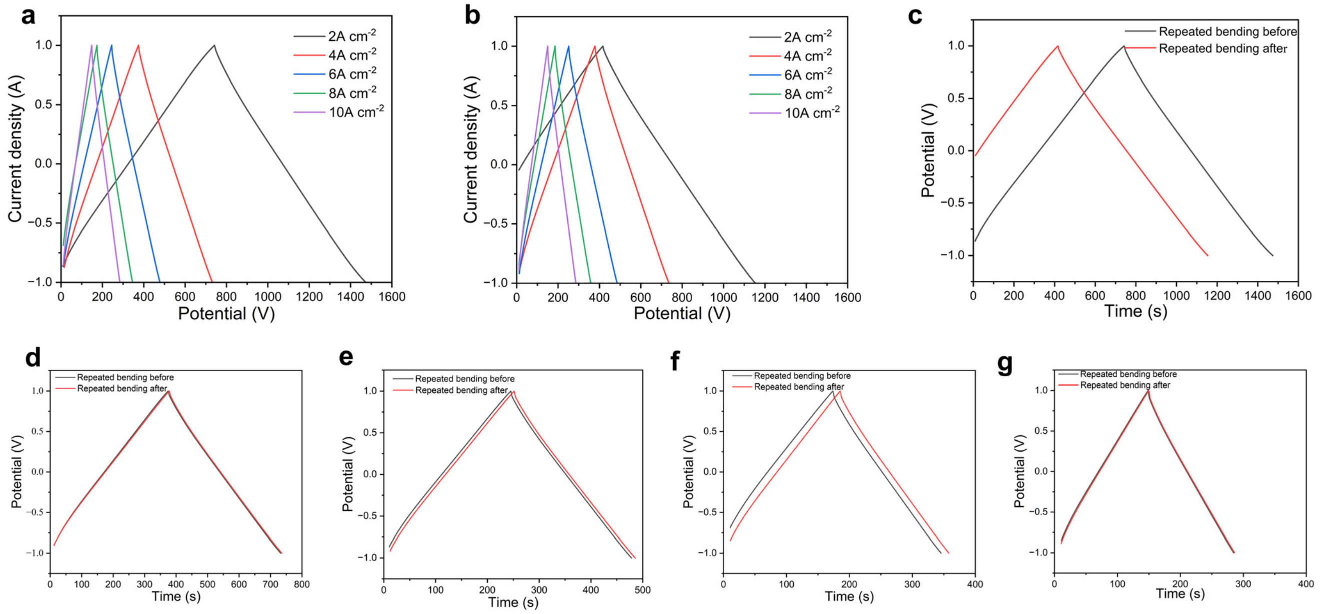

Fig. 13 Galvanostatic charge–discharge (GCD) performance of the flexible supercapacitor before and after repeated bending. (a) Galvanostatic charge–discharge (GCD) curves of the flexible supercapacitor at various current densities (1–10 A cm^{-2}) in the initial unbent state; (b) galvanostatic charge–discharge (GCD) curves of the flexible supercapacitor at various current densities (1–10 A cm^{-2}) after repeated mechanical bending (90° bending angle, 1000 bending cycles); (c–g) comparative GCD curves at current densities of 1, 2, 4, 6, and 10 A cm^{-2}, respectively, where the black curves represent the performance before repeated bending and the red curves represent the performance after repeated mechanical bending (90° bending angle, 1000 bending cycles).

3 Conclusions

In this study, a carboxylation strategy based on TEMPO-mediated oxidation was employed to modify cotton fibers (C-CF), enabling enhanced interfacial compatibility with conducting polymers. The resulting PPy/PANI/C-CF composite electrodes, fabricated *via* sequential *in situ* polymerizations, exhibited improved active material loading, optimized multi-scale pore architecture, and strong fiber–polymer interaction. These structural advantages translated into significantly enhanced electrochemical performance, achieving a high specific capacitance of 911 F g^{-1} at 2 mA cm^{-2} and a capacitance retention of 79.08% after 1000 cycles. This work demonstrates a scalable and effective surface engineering approach for constructing high-performance flexible electrodes, offering practical potential for next-generation wearable and portable energy storage devices. In summary, the structure–performance synergy of PPy/PANI/C-CF composite electrode is realized through the precise regulation of surface chemistry, the rational design of polymer composite and the construction of hierarchical porous structure, which provides a feasible strategy for the preparation of high-performance flexible supercapacitor electrodes based on natural cellulose fibers.

4 Experimental section

4.1 Fabrication of PPy/PANI/C-CF

Sodium *p*-toluenesulfonate (*p*-TSA, >99%, Aladdin Reagent Co., Ltd., China) was first dissolved in deionized water, followed by the addition of pyrrole (Py, >99%, Aladdin Reagent Co., Ltd., China) to formulate a series of Py/*p*-TSA solutions with varying molar ratios of Py : aniline (ANI, >99%, Aladdin Reagent Co., Ltd., China) = 0 : 1, 0.25 : 0.75, 0.5 : 0.5, 0.75 : 0.25, and 1 : 0. Each solution was subjected to ultrasonication to ensure complete mixing. Pre-synthesized PANI/C-CF were immersed in these Py/*p*-TSA solutions for 30 min to allow pre-adsorption of the monomer. Ammonium persulfate (APS, >99%, Aladdin Reagent Co., Ltd., China) was separately dissolved in deionized water to match the molar ratio Py : APS : *p*-TSA = 1 : 1 : 1. The APS solution was slowly added to the monomer-containing dispersion under continuous stirring in an ice bath (≤4 °C), and polymerization was allowed to proceed for 2 h. The resulting composites were thoroughly washed with deionized water to remove unreacted species and dried at 35 °C for 4 h to obtain the PPy/PANI/C-CF hybrid electrodes.

To investigate the influence of dopants, five different dopants—hydrochloric acid (HCl, 37 wt%, Aladdin Reagent Co., Ltd., China), sodium dodecyl benzene sulfonate (SDBS, >99%, Aladdin Reagent Co., Ltd., China), sodium lignosulfonate (>99%, Aladdin Reagent Co., Ltd., China), cetyltrimethylammonium bromide (CTAB, >99%, Aladdin Reagent Co., Ltd., China), and *p*-TSA—were each dissolved in deionized water. Pyrrole was added to each dopant solution, and the mixtures were sonicated. The PANI/C-CF were immersed in these Py-containing dopant solutions for 30 min. APS was again prepared separately, and polymerization was performed as described above, with a fixed molar ratio of Py : APS : dopant = 1 : 1 : 1. To study the effect of dopant concentration, *p*-TSA and Py were dissolved in deionized water with Py : *p*-TSA molar ratios of 1 : 3, 1 : 2, 1 : 1, 2 : 1, and 3 : 1. After ultrasonication, PANI/C-CF composites were immersed in the resulting solutions for 30 min. APS solutions were prepared to ensure a fixed Py : APS molar ratio of 1 : 1. The polymerization and drying processes were carried out using the same protocol as described above.

4.2 Characterization of PPy/PANI/C-CF

The morphology and microstructure of the samples were characterized by field-emission scanning electron microscopy (FE-SEM, Hitachi SU8010, Japan). Elemental distributions were analyzed using energy-dispersive X-ray spectroscopy (EDS) equipped on the same SEM instrument. Optical images of fiber mats before and after polymer deposition were recorded using a digital camera (Canon EOS series).

Fourier-transform infrared (FTIR) spectra were recorded in the range of 4000–500 cm^{-1} on a Bruker Tensor II spectrometer using the KBr pellet method, to confirm chemical group transformation after TEMPO oxidation. X-ray diffraction (XRD) patterns were acquired using a Bruker D8 Advance diffractometer with Cu Kα radiation ($\lambda = 1.5406$ Å) at a scan rate of 2° min^{-1} to analyze crystallinity changes in the cotton fiber substrates before and after surface oxidation.

X-ray photoelectron spectroscopy (XPS, Thermo Fisher ESCALAB 250Xi, USA) was used to investigate surface chemical compositions and bonding states. High-resolution C 1s and N 1 s spectra were deconvoluted to confirm carboxyl group introduction and polymer–substrate interactions. Porosity measurements were conducted *via* a liquid displacement method using ethanol as the penetrant. The porosity (%) was calculated based on the volume difference before and after immersion, according to previously reported procedures.[37]

Electrical conductivity was evaluated by measuring sheet resistance with a four-point probe system (KeithLink FPP-2400, China). The effect of NaClO concentration on conductivity was assessed for both PANI/C-CF and PPy/PANI/C-CF samples. Electrochemical properties were measured using a CHI760E electrochemical workstation (Chenhua, China) in a three-electrode configuration, with the composite electrode as the working electrode, a platinum wire as the counter electrode, and an Ag/AgCl electrode as the reference electrode. Electrolyte: 1.0 M H_2SO_4 aqueous solution. Cyclic voltammetry (CV), galvanostatic charge–discharge (GCD), and electrochemical impedance spectroscopy (EIS) tests were performed. CV scans were conducted at 5–100 mV s^{-1}. GCD measurements were performed at current densities ranging from 2 to 10 mA cm^{-2}. EIS spectra were recorded over a frequency range from 100 kHz to 0.01 Hz with a perturbation amplitude of 5 mV.

4.3 Characterization of PPy/PANI/C-CF flexible electrode materials

Galvanostatic charge–discharge (GCD) tests were conducted on an electrochemical workstation. Symmetric two-electrode devices were assembled with two identical PPy/PANI/C-CF electrodes (1.2 mg cm^{-2} active material loading), current collector, and gel. GCD curves were recorded at 1–10 mA cm^{-2}, and energy density (E) and power density (P) were calculated *via*:

$$E = (1/2) \times C \times (\Delta V^2/3.6)$$

$$P = (E \times 3600)/\Delta t$$

(where C = specific capacitance, ΔV = operating voltage window, Δt = discharge time). A Ragone plot was used to compare with state-of-the-art flexible supercapacitors.

Bending tests (90°, 1000 cycles) evaluated electrode flexibility and electrochemical stability. CV (10 mV s^{-1}) and GCD (2 mA cm^{-2}) measurements were performed before/after bending.

Electrochemical impedance spectroscopy (EIS) was conducted on devices, with an equivalent circuit model (R_s, R_n, W) to analyze impedance behavior and charge/ion transfer characteristics.

Author contributions

Meijuan Cao: investigation, validation, data curation, formal analysis. Xiaopei Wu: methodology, investigation. Dongdong Qiu: methodology, investigation. Shouzheng Jiao: methodology, investigation, validation, data curation, formal analysis, writing – original draft preparation. Jian Sun: conceptualization, supervision, funding acquisition, writing – review & editing. Jie Zong: methodology, investigation, funding acquisition, writing – review & editing.

Conflicts of interest

The authors declare no competing financial interest.

Data availability

The data supporting this article have been included as part of the supplementary information (SI).

Supplementary information is available. See DOI: https://doi.org/10.1039/d5im00294j.

Acknowledgements

This work was financially supported by the National Key R&D Program of China (Grant No. 2023YFE0113800 and 2024YFC3715000), the Natural Science Foundation of Beijing Municipality (Grant No. 8242030), the International Science and Technology Cooperation Base of Green Printing and Publishing Technology (Grant No. KYCPT202506), the Beijing Institute of Graphic Communication Platform Construction Project (Grant No. KYCPT202510), the BIGC Research Project (Grant No. Ec202502), and the Doctoral Research Start-up Fund of Beijing Institute of Graphic Communication (Grant No. Ed2025001).

References

1 Z. Zhao, K. Xia, Y. Hou, Q. Zhang, Z. Ye and J. Lu, Designing flexible, smart and self-sustainable supercapacitors for portable/wearable electronics: From conductive polymers, *Chem. Soc. Rev.*, 2021, **50**, 12702–12743.

2 S. Ye, Y. Zhang, C. An, S. Xiang and G. Wu, Interfacial-aligned and high conductive 1T-MoS_2@$Ti_3C_2T_x$ heterostructure nonwoven fabric for robust deformable supercapacitors, *Adv. Funct. Mater.*, 2025, **35**, 2419779.

3 S. Liu, J. Yang, P. Chen, M. Wang, S. He, L. Wang and J. Qiu, Flexible electrodes for aqueous hybrid supercapacitors: Recent advances and future prospects, *Electrochem. Energy Rev.*, 2024, **7**, 25.

4 Z. Yan, S. Luo, Q. Li, Z. S. Wu and S. Liu, Recent advances in flexible wearable supercapacitors: Properties, fabrication, and applications, *Adv. Sci.*, 2024, **11**, 2302172.

5 S. Zhu, Y. Huang and B. Fang, Progress and prospect for conducting polymer fibers, *Adv. Mater.*, 2025, **37**, e04071.

6 Y. Sood, H. Mudila, P. Chamoli, P. Saini and A. Kumar, Exploring the efficacy and future potential of polypyrrole/metal oxide nanocomposites for electromagnetic interference shielding: A review, *Mater. Horiz.*, 2024, **11**, 4256–4274.

7 X. Han, C. Hao, Y. Peng, H. Yu, T. Zhang, H. Zhang, K. Chen, H. Chen, Z. Wang and N. Yan, Novel cellulosic fiber composites with integrated multi-band electromagnetic interference shielding and energy storage functionalities, *Nano-Micro Lett.*, 2025, **17**, 122.

8 M. Shi and X. Zhang, Pioneering the future: Principles, advances, and challenges in organic electrodes for aqueous ammonium-ion batteries, *Adv. Mater.*, 2025, **37**, 2415676.

9 Q. Zeng and Z. Huang, Challenges and opportunities of implantable neural interfaces: From material, electrochemical and biological perspectives, *Adv. Funct. Mater.*, 2023, **33**, 2301223.

10 P. M. Jambhale, V. N. Narwade, M. Shariq, K. A. Bogle and M. D. Shirsat, Waste to wealth: Upcycling waste toner into magnetic Fe_3O_4 and conducting polymer hybrids for enhanced energy storage application, *J. Electron. Mater.*, 2024, **53**, 3117–3127.

11 Y. Qiao, H. Jia, Y. Zhang, W. Zhao, E. Zhang, S. Zhang, X. Jian and C. Liu, Comprehensive evaluation of interfacial interactions optimization for CF reinforced high-performance thermoplastic composites by electrochemical deposition of conjugated polymers, *Compos. Sci. Technol.*, 2024, **258**, 110863.

12 A. S. Nitai, T. Chowdhury, M. N. Inam, M. S. Rahman, M. I. H. Mondal, M. Johir, V. Hessel, I. M. R. Fattah, M. A. Kalam and W. A. Suwaileh, Carbon fiber and carbon fiber composites—creating defects for superior material properties, *Adv. Compos. Hybrid Mater.*, 2024, **7**, 169.

13 Y. Sun, C. Li, D. Liu, F. Zhang, J. Xue and Q. Zheng, Surface and interfacial engineering for multifunctional nanocarbon materials, *ACS Nano*, 2025, **19**, 1944–1980.

14 T. Xu, H. Du, H. Liu, W. Liu, X. Zhang, C. Si, P. Liu and K. Zhang, Advanced nanocellulose-based composites for flexible functional energy storage devices, *Adv. Mater.*, 2021, **33**, 2101368.

15 P. Chen, X. Lin, B. Yang, Y. Gao, Y. Xiao, L. Li, H. Zhang, L. Li, Z. Zheng and J. Wang, Cellulose separators for rechargeable batteries with high safety: Advantages, strategies, and perspectives, *Adv. Funct. Mater.*, 2024, **34**, 2409368.

16 B. Thomas, M. C. Raj, A. K. B, J. Joy, A. Moores, G. L. Drisko and C. Sanchez, Nanocellulose, a versatile green platform: From biosources to materials and their applications, *Chem. Rev.*, 2018, **118**, 11575–11625.

17 L. Solhi, J. Li, J. Li, N. M. Heyns and H. Brumer, Oxidative enzyme activation of cellulose substrates for surface modification, *Green Chem.*, 2024, **26**, 4026–4040.

18 V. Rahmanian, T. Pirzada, S. Wang and S. A. Khan, Cellulose-based hybrid aerogels: Strategies toward design and functionality, *Adv. Mater.*, 2021, **33**, 2102892.

19 M. Manimaran, M. N. Norizan, M. H. Mohamad Kassim, M. S. Salit, M. N. F. Norrahim, M. R. Adam and A. I. Rushdan, Functionalization and performance of hybrid nanocellulose from plant-based/metal oxide nanocomposites for sustainable energy applications, *Phys. Sci. Rev.*, 2025, **10**, 151–198.

20 A. Isogai, TEMPO-catalyzed oxidation of polysaccharides, *Polym. J.*, 2022, **54**, 387–402.

21 S. Liu, Z. X. Low, Z. Xie and H. Wang, TEMPO-oxidized cellulose nanofibers: A renewable nanomaterial for environmental and energy applications, *Adv. Mater. Technol.*, 2021, **6**, 2001180.

22 F. P. Wang, J. J. Li, Y. Zhang, M. Y. Sun, L. Li, F. Wahid, Y. Y. Xie, S. Jia, W. Li and C. Zhong, TEMPO-mediated oxidation promotes cellulose dissolution in a zincate–NaOH system at suprazero temperatures, *ACS Sustainable Chem. Eng.*, 2022, **10**, 7374–7384.

23 J. Chen, Q. Peng, X. Peng, H. Zhang and H. Zeng, Probing and manipulating noncovalent interactions in functional polymeric systems, *Chem. Rev.*, 2022, **122**, 14594–14678.

24 S. Kim, J. Baek, J. I. Choi, Y. R. Jo, S. S. Jang and G. H. An, High-adhesion zinc anode protective film with metal-ion-doped conductive polymer-coated carbon nanotubes for zinc ion batteries, *Nano Energy*, 2025, **142**, 111203.

25 R. Liu, L. Hou, G. Yue, H. Li, J. Zhang, J. Liu, B. Miao, N. Wang, J. Bai and Z. Cui, Progress of fabrication and applications of electrospun hierarchically porous nanofibers, *Adv. Fiber Mater.*, 2022, **4**, 604–630.

26 R. Shi, Y. Tian and L. Wang, Bioinspired fibers with controlled wettability: From spinning to application, *ACS Nano*, 2021, **15**, 7907–7930.

27 Y. Yuan, L. Wu, B. Yan, Y. Yu, Q. Wang and P. Wang, Fabrication and efficient interfacial assembly of bright red-emitting carbon quantum dots for security-warning textiles, *Small*, 2024, **20**, 2405101.

28 Z. Li, W. Hu, J. Dong, F. Azi, X. Xu, C. Tu, S. Tang and M. Dong, The use of bacterial cellulose from kombucha to produce curcumin loaded Pickering emulsion with improved

stability and antioxidant properties, *Food Sci. Hum. Wellness*, 2023, **12**, 669–679.

29 J. Wei, Q. Ma, Y. Teng, T. Yang, K. H. Wong, Y. Cui, B. Zheng, D. Li, D. Luo and A. Yu, Advanced cellulosic materials toward high-performance metal ion batteries, *Adv. Energy Mater.*, 2024, **14**, 2400208.

30 L. Chen, L. Yu, L. Qi, S. J. Eichhorn, A. Isogai, E. Lizundia, J. Zhu and C. Chen, Cellulose nanocomposites by supramolecular chemistry engineering, *Nat. Rev. Mater.*, 2025, **10**, 728–749.

31 C. Zheng, Y. Guo, C. Zhang, X. Cao and J. Wan, Nitrogen-defective protonated porous C_3N_4 nanosheets for enhanced photocatalytic hydrogen production under visible light, *Appl. Catal. B Environ. Energy*, 2025, **365**, 124879.

32 L. Malfatti, M. Poddighe, L. Stagi, D. Carboni, R. Anedda, M. F. Casula, B. Poddesu, D. De Forni, F. Lori and S. Livraghi, Visible light activation of virucidal surfaces empowered by pro-oxidant carbon dots, *Adv. Funct. Mater.*, 2024, **34**, 2404511.

33 F. Zhang, P. C. Sherrell, W. Luo, J. Chen, W. Li, J. Yang and M. Zhu, Organic/inorganic hybrid fibers: Controllable architectures for electrochemical energy applications, *Adv. Sci.*, 2021, **8**, 2102859.

34 Y. Wu, M. Wang, Y. Tao, K. Zhang, M. Cai, Y. Ding, X. Liu, T. Hayat, A. Alsaedi and S. Dai, Electrochemically derived graphene-like carbon film as a superb substrate for high-performance aqueous Zn-ion batteries, *Adv. Funct. Mater.*, 2020, **30**, 1907120.

35 K. Jayaramulu, D. P. Dubal, B. Nagar, V. Ranc, O. Tomanec, M. Petr, K. K. R. Datta, R. Zboril, P. Gómez-Romero and R. A. Fischer, Ultrathin hierarchical porous carbon nanosheets for high-performance supercapacitors and redox electrolyte energy storage, *Adv. Mater.*, 2018, **30**, 1705789.

36 K. Guo, L. Bao, Z. Yu and X. Lu, Carbon encapsulated nanoparticles: Materials science and energy applications, *Chem. Soc. Rev.*, 2024, **53**, 11100–11164.

37 K. Xie, N. Wang, Y. Guo, S. Zhao, J. Tan, L. Wang, G. Li, J. Wu, Y. Yang and W. Xu, Additively manufactured biodegradable porous magnesium implants for elimination of implant-related infections: An in vitro and in vivo study, *Bioact. Mater.*, 2022, **8**, 140–152.